



HAL
open science

Electrochemical investigation of ceria nanoparticles as corrosion inhibitor for steel in alkaline medium

Nadjette Bourenane, Youcef Hamlaoui, Fernando Pedraza

► **To cite this version:**

Nadjette Bourenane, Youcef Hamlaoui, Fernando Pedraza. Electrochemical investigation of ceria nanoparticles as corrosion inhibitor for steel in alkaline medium. *Materials and Corrosion / Werkstoffe und Korrosion*, 2023, 74 (9), pp.1356-1370. 10.1002/maco.202313821 . hal-04458103

HAL Id: hal-04458103

<https://hal.science/hal-04458103>

Submitted on 14 Feb 2024

HAL is a multi-disciplinary open access archive for the deposit and dissemination of scientific research documents, whether they are published or not. The documents may come from teaching and research institutions in France or abroad, or from public or private research centers.

L'archive ouverte pluridisciplinaire **HAL**, est destinée au dépôt et à la diffusion de documents scientifiques de niveau recherche, publiés ou non, émanant des établissements d'enseignement et de recherche français ou étrangers, des laboratoires publics ou privés.

Electrochemical investigation of ceria nanoparticles as corrosion inhibitor for steel in alkaline medium

N. Bourenane¹, Y. Hamlaoui^{1*}, F. Pedraza².

1 Laboratoire de Physique de la Matière et Rayonnement (LPMR), Faculté des Sciences et de Technologie, Université Mohamed Chérif Messaadia, BP 1553, 41000 Souk-Ahras, Algérie.

2 Laboratoire de Sciences de l'Ingénieur pour l'Environnement (LaSIE), UMR 7356 CNRS Institut LUDI, La Rochelle Université, Avenue Michel Crépeau, 17042 La Rochelle Cedex 1, France.

* Corresponding author: hamlaoui_youcef@yahoo.fr

Abstract

This work investigates the synthesis and the corrosion inhibitor efficiency ceria nanoparticles may exert on steel reinforcement in alkaline solution of saturated $\text{Ca}(\text{OH})_2 + 0.5\text{M CaCl}_2$ up to 50 °C. The corrosion mechanisms are thoroughly investigated by electrochemical and various characterization techniques. The electrochemical results show that ceria nanoparticles act as anodic inhibitor and provide maximum inhibition efficiency (80 %) at a concentration of 800 ppm. The resulting surface is smooth and free from corrosion products due to the formation of a physically adsorbed film according to the thermodynamic calculations.

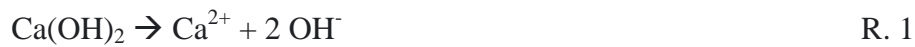
Keywords: ceria nanoparticles, alkaline medium, corrosion inhibition, surface morphology, bath temperature.

1.- Introduction

Corrosion of reinforcing steel, which occurs when chloride ions migrate through the concrete pores is considered as the most important cause that determines the durability of reinforced concrete structures. This type of corrosion often occurs in buildings and most highway bridges which are usually constructed with rebar reinforcing steel. The cement paste through which the contaminants initiate the process determines the corrosion resistance of steel reinforcing bars [1]. During hydration, Portland cement reacts chemically with water where the anhydrous compounds, which are slightly soluble, dissolve in solution to give different ionic species. The main hydration products are calcium-silicate-hydrate “C-S-H”, and Portlandite or $\text{Ca}(\text{OH})_2$ “C-H” where the amount of C-S-H or $\text{Ca}(\text{OH})_2$ depend mainly on the water/cement ratio and the hydration time [2-3].

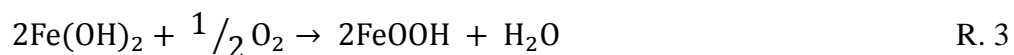
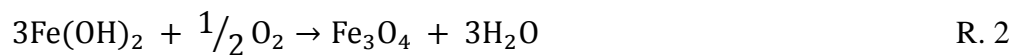
A cement paste hardened in ordinary conditions contains between 50 and 70 % of C-S-H and 25 to 27 % of $\text{Ca}(\text{OH})_2$. The C-S-H is the most important hydrated phase in the hardened cement that the main mechanical properties of the material will depend on. However, Portlandite is the compound that determines the concrete alkalinity (pH of concrete is between 12.4 and 13.5) and may lower the physical properties of the cement paste since it is more soluble than the C-S-H gels. However, Portlandite adjusts the interstitial solution pH value to approximately 12.5. When this phase is completely solubilized, the C-S-H fixes the solution pH between $10.5 < \text{pH} < 12.5$. It is therefore the most soluble phase that imposes the pH until its total dissolution [4]. It is noted that the interstitial solution contains cations such as Ca^{2+} , Na^+ and K^+ and anions such as SO_4^{2-} and OH^- . Calcium ions come from gypsum and portlandite whereas sodium and potassium ions are derived from alkaline oxides (Na_2O and K_2O) present in cement. In addition, such cations can come from contamination agents (chlorides or sulphates) and/or from water [5]. Nevertheless, the presence of portlandite fixes

the pH at 12.5 and the calcium concentration at 21 mmol/kg according to the equilibrium reaction R. 1:



The most employed solutions to reproduce the chemical characteristics of concrete are alkaline solutions with Ca(OH)_2 at saturation with and without NaOH, KOH and carbonate-based solution (NaHCO_3 , Na_2CO_3) for uncontaminated or for carbonated concrete, respectively [6-8]. Indeed, alkaline solutions in the presence of chloride ions in the form of NaCl or CaCl_2 were used to study the electrochemical behaviour and the depassivation mechanism [9] whereas buffered carbonate solutions are rarely used to study the corrosion behaviour of steel reinforcement in concrete [10].

It is well-known that the corrosion mechanism of steel in concrete involves two steps. The first step consists in the oxidation of the steel where the released Fe^{2+} ions combine with OH^- resulting from the cathodic reaction to give rise to the ferrous hydroxide Fe(OH)_2 . This reaction is favoured by the high alkalinity (pH values > 12.5) of the pore solution near the surface of the steel which usually occurs in uncontaminated concrete. Ferrous hydroxide Fe(OH)_2 react with water and oxygen to form hydrated ferric oxide ($\text{Fe}_2\text{O}_3 \cdot \text{H}_2\text{O}$), hydrated magnetite ($\text{Fe}_3\text{O}_4 \cdot \text{H}_2\text{O}$), or evolve into goethite ($\alpha\text{-FeOOH}$) or lepidocrocite ($\gamma\text{-FeOOH}$) according to the reactions R. 2 and R. 3 [11]:



The exposure of reinforced concrete to chloride ions is the primary cause of premature corrosion of steel reinforcement. The intrusion of chloride ions from seawater or present in water or aggregate used in concrete, into reinforced concrete can cause steel corrosion if

oxygen and moisture are also available to sustain the reaction. Chlorides dissolved in water can permeate through sound concrete or reach the steel through cracks. Thus, when the chloride content at the surface of the steel exceeds a certain limit known as the chloride threshold value, corrosion will occur if water and oxygen are also available. Although chlorides are directly responsible for the initiation of corrosion, they appear to play only an indirect role in the rate of corrosion after initiation. The primary rate-controlling factors are the availability of oxygen, the electrical resistivity and saturation degree of the concrete as well as pH and temperature.

Several studies have been conducted to develop methods and products to reduce or even to arrest the corrosion of steel reinforced concrete [12-14] including among others, cathodic protection [3, 15] (usually used for chloride contaminated concrete structures and for which it is necessary to keep the original surface [15]), surface oxidation [16], epoxy coating [17-18], electrochemical re-alkalization and electrochemical chloride extraction (ECE) [19]. Yet, the use of organic and inorganic corrosion inhibitors is considered to be the simplest and the least expensive [20].

In this view, cerium salts were successfully applied as corrosion inhibitors for metals in NaCl solution mainly for Al [21], Mg [22], Zn [23], carbon steel [24-26] and for Zn and rebar steel in concrete [27, 28]. Ceria deposited films act as a physical barrier which prevent dissolved O_2 and or aggressive anions such as Cl^- and SO_4^{2-} to penetrate through defects or cracks to the surface of the substrate. Moreover, it was shown that ceria based coatings repair defects after being damaged through Ce^{3+}/Ce^{+4} redox process. The exchange process $2 CeO_2 \leftrightarrow Ce_2O_3 + 1/2 O_2$ is favoured since the redox reaction $Ce^{4+} \leftrightarrow Ce^{3+}$ occurs easily [29-31]. Thus, following the success of cerium salts used as corrosion inhibitor, ceria particles have also been widely studied as pigments in organic protective coatings [32-34], as corrosion inhibitor of Zn [35], of steel in Na_2SO_4 solution [36], in HCl and H_2SO_4 [37]. To the best of

our knowledge, only very limited work was conducted on the effectiveness of ceria nanoparticles as corrosion inhibitor in concrete pore solution [38]. Therefore, in the current study, the corrosion behaviour of steel is examined during immersion in alkaline solution of saturated lime $\text{Ca}(\text{OH})_2$ contaminated by CaCl_2 chloride ions containing ceria nanoparticles as corrosion inhibitor. Also, the effect of the temperature on the inhibition efficiency of the inhibitor was evaluated between 25 and 55°C. For all such purposes, electrochemical techniques and surface morphological characterization were conducted.

2.- Experimental set-up

2.1.- Materials

Reinforcing steel bar of 10 mm in diameter according to E24 specification (NF EN 10025) with chemical composition C-0.17, Mn-1.4, P-0.045, S-0.045 N-0.009 and balance Fe, was used. Coupon samples of 10-mm of diameter were cut from the steel bar. The active surface of the electrode was polished using a series of SiC papers ranging from 180 to 2500 grit, degreased by sonication for 30 min in acetone and then with ethanol, rinsed several times with distilled water and finally dried with hot air. The samples were kept in desiccators until immersion.

2.2.- Synthesis of ceria nanoparticles.

Cerium nitrate ($\text{Ce}(\text{NO}_3)_3 \cdot 6\text{H}_2\text{O}$, Strem, 99,9 %) and acetic acid as organic ligand were used for nanoceria synthesis in colloidal dispersion. More details can be found in recent research involving the use of dispersion colloids for ceria preparation in the references [39-41]. In a double-envelope stirred reactor, 0.5 M cerium nitrate and 0.5 M acetic acid were dissolved in 100 ml distilled water at 60 °C. 24.5 % ammonia was slowly added drop by drop to the above solution until reaching a pH solution equal to 9 then the bath temperature was increased to

90 °C. Right after, the reactor was hermetically closed in order to reduce the amount of the dissolved oxygen almost to 50 %. After 24 hours of stirring, the precipitate was recovered by centrifugation at 4000 rpm during 50 minutes in the presence of excess ethanol. The resulting precipitate was washed and centrifuged with distilled water and ethanol alternately three times in order to eliminate residual ions such as acetate. Finally, the collected ceria nanoparticles were redispersed in distilled water to constitute the inhibitor with a content of 10 wt% of ceria nanoparticles.

It was noted that during the addition of ammonia to alkalize the medium, changes of the solution colours occur depending on the pH of the solution (Figure 1): for $\text{pH} < 3.4$, the solution is transparent (Fig. 1.a), a light brown coloration characteristic of $\text{Ce}(\text{OH})_3$ precipitate subsequently appeared (Figures 1.b and 1.c). For solution pH maintained between 9 and 9.5 (Fig. 1.d and 1.e), the colour of the medium becomes violet characterizing an oxidation reaction of $\text{Ce}(\text{OH})_3$ to $\text{Ce}(\text{OH})_4$ with a very significant increase of the medium viscosity. After 24 h of reaction time, the solution turns into a pale yellow colour (Fig. 1.f).

2.3.- Electrochemical Tests

A conventional three-electrode cell was used with a saturated calomel electrode as reference electrode, a platinum wire as counter electrode and the steel rebars as working electrode. Electrochemical tests were carried out with a potentiostat Biological SP 150 Instrument at room temperature (21 ± 2 °C). $\text{Ca}(\text{OH})_2$ saturated solution was prepared with 3 g L^{-1} of $\text{Ca}(\text{OH})_2$ in distilled water. The pH was 12.6. The concentration of the chloride ions in the solution was 0.5 M. Polarization resistance, R_p , was obtained from the slope of potentiodynamic scan carried out in the anodic direction from -20 to +20 mV vs E_{oc} (open circuit potential) at scan rate of 0.5 mV/s.

The potentiodynamic polarization curves were obtained by using a sweep rate of 0.5 mV/s between $E_{oc} \pm 250$ mV. The impedance data were obtained at the E_{oc} between 100 kHz and 10 mHz, with 4 mV as the applied sinusoidal perturbation. The EIS response from the samples was fitted using ZView software (Scribners Associates, USA). The potentiodynamic polarization and EIS techniques were performed after 30 min of immersion time.

2.4.- Characterization

Non- contact white- light optical profilometry was performed using a WLI FRT. Imaging of the surface of the samples was conducted using vertical scanning interferometry (VSI) mode with full resolution. Analysis of the surface roughness, thickness, and grain size was done using FRT Mark III software (FormFactor Inc). Surface analysis was also performed using a Zeiss Axio Imager M1 Trinocular Frame optical microscope. Moreover, the surface morphology was analyzed more thoroughly using a scanning electron microscope (SEM) of FEI Quanta 250 equipped with X- ray energy- dispersive spectroscopy (EDS) for chemical analysis of films.

3.- Results and discussion

3.1.- Ceria nanoparticles

The SEM image of the synthesized ceria nanoparticles (Figure 2.a) shows a homogeneously distributed non-spherical shaped morphology with a diameter of agglomerated particles around of 70 nm, which is in good agreement with previous works [42,43]. Besides, a few clusters were also identified in the SEM image, which exhibits irregularly shaped and large sized particle aggregates. The FT-IR spectrum in Fig. 2.b shows the characteristic chemical bands of synthesized CeO_2 nanoparticles. The observed bands are in good agreement with the literature [44] where the intense absorption band appearing at 3227 cm^{-1} is characteristic for

the OH bond of the carboxylic acid and water. The bands observed at 2824 and 2816 cm^{-1} are attributed to the C-H bond. The band at 2359 cm^{-1} is not well defined and is due to the absorption of atmospheric CO_2 . The bands appearing in the range between 594 and 668 cm^{-1} are related to asymmetric and symmetric vibrations of Ce-O. Other bands corresponding to Ce-O are observed at 843 cm^{-1} and between 917 and 1558 cm^{-1} .

3.2.- Corrosion inhibition at room temperature

Fig. 3 depicts the polarization curves for the substrate in the corrosive medium with and without inhibitor addition at room temperature. Table 1 summarizes the corrosion parameters including the corrosion potential (E_{corr}), the corrosion current densities (i_{corr}) and the anodic and cathodic Tafel slopes (β_a and β_c) obtained from the polarization plots by extrapolating the linear portion of the curve. The efficiency of inhibition (EI (%)) was calculated using the following equation (Eq. 1) and the obtained values are listed in Table 1.

$$\text{EI (\%)} = \left(1 - \frac{i_{\text{corr}}(\text{inh})}{i_{\text{corr}}}\right) \times 100 \quad \text{Eq. 1}$$

Where i_{corr} et $i_{\text{corr}}(\text{inh})$ are the corrosion current density without and with inhibitor addition, respectively.

As shown in Fig. 3, the corrosion potential of the substrate shifted towards more cathodic values for inhibitor concentrations of 100 and 200 ppm. Yet, the Tafel slopes are similar to those of the blank material, i.e. with no inhibitor. This implies that low concentrations of inhibiting nanoparticles do not markedly develop any passive layer or ensure any improvement of the corrosion resistance as also described in previous works for Al alloys [32] and steel [36]. However, for inhibitor concentrations higher than 200 ppm, the anodic slopes shifted the E_{corr} towards anodic values thereby suggesting that ceria nanoparticles act as an anodic inhibitor. This feature can be explained in terms of the nature of the formed layer

which provides a “physical barrier” possibly promoted by oxidation of the substrate upon the reduction of Ce^{4+} into Ce^{3+} following reaction R. 4 as also proposed by Li et al. [45].



It is well known that CeO_2 is suitable for the storage and the release of oxygen under varying conditions between reduced and oxidized state of cerium ions [45]. The passivation mechanism in this case can be explained by a prior adsorption of the particles followed by a redox process in which the reduction of the passivating anion takes place on the defects located on the surface of the oxide and hydroxide layer [43, 46]. The electrochemical parameters calculated from polarization curves (Table 1) show an increase of the inhibition efficiency with increasing the inhibitor concentration reaching 78% for 800 ppm, which corresponds to the minimum effective concentration “MEC”.

To confirm such MEC at 800 ppm, the more sensitive electrochemical impedance spectroscopy (EIS) diagrams were conducted at the OCP (Fig. 4). The Nyquist plot (Fig. 4.a) shows that the substrate immersed in the blank solution displays two capacitive loops but the impedance arc is flattened at intermediate frequencies. This phenomenon is usually caused by the constant phase element (CPE) [47]. Moreover, the impedance spectra did not show a perfect semi-circle. Similarly, the Bode diagrams clearly show phase angle values far from -90° (Fig. 4.b). Therefore, the equivalent circuit shown in Fig. 5a to fit the EIS plots contains a solution resistance “ R_s ” in series with two time constants. The capacitive loop at high frequencies is attributed to outer porous layer (R_c - CPE_c) and the second one at low frequencies reflects the charge transfer reaction of the steel substrate (R_{ct} - CPE_{dl}). Where R_c , R_{ct} , represent the layer and charge transfer resistance. CPE_c (constant phase element) and CPE_{dl} are the non-ideal layer capacitance and double layer capacitance respectively. The exponent n ($0 < n < 1$) is a non-linear coefficient which varies with the electrode surface roughness. The presence of the CPE instead of a capacitance indicates dispersion effects by

imperfections and roughness of surface. In contrast, the diagrams for the substrate in the corrosive solution with inhibitor addition were fitted using an equivalent circuit “EC” composed of three-time constants (Fig. 5b) where the not well defined straight line at low frequencies is attributed to an initiation of a diffusion process (Warburg resistance “ Z_w ”) induced by oxygen diffusion as reported by Eichler et al. [48] and or by the evolution of a redox process attributed to Ce oxide (reaction R. 4). Except for the EIS diagrams performed in the solution with small amount of the inhibitor added (less than 200 ppm) where no inhibition efficiency was shown, the diameter of the semi-circle in the Nyquist plots (giving information about the global resistance) increases with increasing the inhibitor concentration to reach its maximum value at 800 ppm and decreases afterwards. The linear polarization resistance values (Table 1) evaluated at low frequencies give more significant information about the global resistance. Indeed, it appears from the EIS diagrams that the polarization resistance at low frequencies increased more than 3 times for the solution with the addition of 800 ppm than in the inhibitor free solution. Furthermore, the Bode plots show that the maximum (θ_{max}) shifts slightly toward lower frequencies with increasing inhibitor concentration from 200 to 800 ppm. In summary, it is found that θ_{max} increases from 73° to 82° for, respectively the solution without and with 800 ppm of inhibitor, which is indicative of an increase of the capacitive behaviour and that the film becomes more protective.

The main EIS parameters are gathered in Table 2. It can be noted that the EI% inhibition efficiency of the EIS technique was calculated by comparing the values of R_{ct} of the substrate in $Ca(OH)_2$ and 0.5 M $CaCl_2$ without and with inhibitor addition according to equation Eq. 2.

$$EI (\%) = \left(1 - \frac{R_{ct}}{R_{ct}(inh)} \right) \times 100 \quad \text{Eq. 2}$$

Table 2 shows that the minimum effective concentration corresponds to 800 ppm, which is in good agreement with d.c polarization results. The increase of the layer resistance “ R_c ” with

the increase of the inhibitor concentration (Table 2) suggests that the inhibitor delays the degradation of the substrate through the formation of a protective layer on the surface, which decreases the active surface area. Besides, the decrease in the inhibitor film capacitance indicates an increase of the film thickness. Furthermore, the increase in charge transfer resistance (R_{ct}) and the decrease of the double layer capacitance values CPE_{dl} with increasing the concentration of inhibitor indicate the absence of interfacial dispersion [48-50]. This is likely due to a precipitation of the cerium oxides in the defects of the film, which block the anodic active sites.

The surface morphology of the substrate after polarization tests in the aggressive medium with and without inhibitor addition was evaluated by optical microscopy, scanning electronic microscopy and white light interferometry. As shown in Fig. 6, the surface of the substrate in the blank solution undergoes severe degradation (black spots) that gradually diminishes with the inhibitor addition. The surface of the substrate after polarization in the aggressive medium with 800 ppm of inhibitor seems to be free from corrosion products, which is in good agreement with the electrochemical results. The same morphology is also observed with SEM images (Fig. 7). Except for the samples polarized in the presence of 600 and 800 ppm of the inhibitor, all other surfaces were not smooth and showed the presence of pores, which indicates that the samples undergo localized corrosion. This is in good agreement with another study showing that pitting corrosion starts on pores of the passive layer formed in chloride containing concrete solution [51].

The EDS analysis of the film formed on the surface of the substrate treated in the aggressive medium with 800 ppm shows that the film is composed of iron, oxygen and calcium. In addition, cerium was also detected. These results confirm that the protective formed film on the surface of the steel is composed of a mixture of the corrosion products and ceria nanoparticles. To confirm this behaviour, the morphology of the surface of the substrate was

also examined by using the white light interferometer. The 3D images (Fig. 8) and the calculated parameters of the film are gathered in Table 3. It can be clearly seen that the overall surfaces of the substrates in the presence of the inhibitor are considerably smoother and free from dark spots (black areas is attributed to the surface of the substrate which means lower thickness) compared to the surface of the substrate in the blank solution. The calculated surface parameters (Table 3) showed that the higher average thickness and maximum grain size is observed for the substrate treated with 800 ppm of ceria nanoparticles. However, the average roughness values calculated with the FRT Mark III software, decreases continuously with increasing inhibitor concentration, which is attributed to the formation of homogenous and smooth ceria-iron oxides protective films. Iron oxides are the result of the substrate dissolution occurring before or simultaneously with ceria deposition leading to an increase of the grain size of the film particles (Table 3) as also proposed in other investigations [52,53].

3.2.- Effect of bath temperature

The temperature of the corrosive baths is an important parameter influencing the corrosion rate and the inhibition efficiency as well as modifying the mechanism of the adsorption of the inhibitor on the electrode surface [54]. In order to evaluate the effect of the temperature of the solution on the corrosion inhibition efficiency of ceria nanoparticles, the tests were carried out at bath temperatures ranging from 20 to 50 °C without and in the presence of the optimal concentration of ceria nanoparticles (800 ppm). The evaluation of the inhibition efficiency was firstly investigated by potentiodynamic polarization techniques as shown in Figure 9. In the non-inhibited solution, the evolution of corrosion currents densities i_{corr} and anodic Tafel slopes with increasing bath temperature shows a continuous increase (Table 4) as a result of an increase of the metal dissolution reaction. In contrast, the cathodic slopes remain practically constant irrespective of temperature, which may indicate that the oxygen reduction

reaction occurs with the same activation mechanism. On the other hand, the increase of i_{corr} with increasing bath temperature of the inhibited solution with ceria nanoparticles seems to be significantly lower than the one observed in the blank solution. Moreover, the inhibitor remains effective in the studied temperature range (see Table 4). According to Boudelloua et al. [55], the difference in the decrease of i_{corr} values in inhibited and blank solution is mainly due to the film formed on the surface of the substrate.

It should also be noted that the recovery rate (θ) calculated from Eq. 3 dropped by about 50 % when the bath temperature increased from 40 to 50 °C, thereby indicating a decrease in the inhibition efficiency.

$$\theta = 1 - \frac{i_{corr}(inh)}{i_{corr}} \quad \text{Eq. 3}$$

According to Mobin et al. [56], this decrease in the inhibition efficiency could be attributed to the intensification of thermal agitation and to the increase of the solution conductivity of the environment, hence the corrosivity of the medium. The drop on recovery rate would be in line with the works from Ngala et al. [57] and Rosenberg and coll. [58], who suggested that the inhibitor is physically adsorbed, hence the physisorption process predominates. The hypothesis was assessed by calculating the activation energy where the variation of the corrosion current densities with the temperature is expressed by the Arrhenius law (Eq. 4):

$$\ln(i_{corr}) = \ln A - \frac{E_a}{R} \left(\frac{1}{T}\right) \quad \text{Eq. 4}$$

Where E_a is the activation energy, R is the ideal gas constant, A is the Arrhenius constant and T is the absolute temperature.

The development of the Arrhenius equation (Eq. 5) in its useful form (Eq. 6) makes it possible to determine the enthalpy “ ΔH_a ” and the entropy “ ΔS_a ” of adsorption [59].

$$I_{corr} = \frac{RT}{N_h} \exp\left(\frac{\Delta S_a}{R}\right) \exp\left(-\frac{\Delta H_a}{RT}\right) \quad \text{Eq. 5}$$

$$\ln \frac{I_{corr}}{T} = -\frac{\Delta H_a}{RT} + \ln \frac{R}{N_h} + \left(\frac{\Delta S_a}{R}\right) \quad \text{Eq. 6}$$

where N is Avogadro's number and h is Planck's constant. ΔS and ΔH are respectively, the entropy and enthalpy of activation for the adsorption to occur.

Figure 10 shows the graphical representation of the Arrhenius law under both forms Eq. 5 and Eq. 6 of the steel substrate immersed in saturated calcium hydroxide solution and 0.5 M of CaCl_2 with and without inhibitor addition. The obtained thermodynamic parameters are summarized in Table 5. The calculated values show that E_a for the substrate immersed in the aggressive medium with inhibitor addition is greater than that in absence of inhibitor, which is defined as the additional energy necessary for the formation of the protective film [60]. On other hand, the weak positive values of ΔH_a reveals that the ceria nanoparticles adsorb on the surface of mild steel through an endothermic physisorption process as it involves formation of electrostatic weak bonds generated at the surface of the substrate [61].

Furthermore, the changes in entropy (ΔS_a) imply that the activated complex represented the rate-determining step for the association rather than the dissociation step [62]. According to Popova et al. [63] when the inhibition efficiency decreases as bath temperature increases, it indicates the presence of a few active sites blocked by the adsorbed inhibitor and in this case the activation energy in the inhibited solution becomes higher compared to the free solution.

The surface of the metal immersed in saturated calcium hydroxide solution and 0.5 M of CaCl_2 without and with 800 ppm of ceria nanoparticles was characterized by SEM (Fig. 11). The SEM images clearly show a very heterogeneous structure of the surface of the substrate immersed in the aggressive medium without inhibitor. The samples indeed seem to undergo a pitting attack well observed at bath temperature 40 °C (Fig. 11.a). However, in the inhibited solution, the micrographs presented in Figure 11.b reveal a uniform and thin protective film free from cracks or defects. With increasing solution temperature the surface appeared less smooth and more cracked indicating that the deposited film became less resistant against

corrosion, although it still remains effective compared to the uninhibited solution. Based on the surface morphologies and the electrochemical results, it seems that the precipitation of the ceria nanoparticles inside the initiated pits diminishes their rate of propagation and blocks the initiation of cracks. However, when the bath temperature increases, the holes appear more frequently and seem to reach a critical size where cracks can initiate. According to Zand et al. [64], the coating defects may serve as initiators for pit corrosion through reduced coating thickness and/or as the initiation sites of fatigue cracks. It should be noted that even by increasing the bath temperature the behaviour of the substrate in the inhibited solution remains better compared to that in the uninhibited solution.

4.- Conclusions

In this study, the electrochemical behaviour of a E24 (NF EN 10025) rebar steel immersed in saturated $\text{Ca}(\text{OH})_2$ with 0.5 M CaCl_2 with and without ceria nanoparticles as corrosion inhibitor was investigated. Thereafter, the inhibitor efficiency was evaluated and the effect of the bath temperature on it. A significant corrosion inhibition effect leading to a high polarization resistance compared to the uninhibited solution was observed. The maximum inhibition efficiency (about 80 %) was obtained when adding 800 ppm of ceria nanoparticles to the corrosive medium. The EIS diagrams showed the initiation of a new relaxation time attributed to a diffusion process. The surface morphology of the substrate immersed in the aggressive medium underwent localized corrosion, whereas with the addition of 800 ppm of ceria nanoparticles smooth surfaces, free from corrosion products were obtained. The surface parameters deduced in the studied bath temperature range showed that the inhibitor remains effective despite the increase of the corrosion current densities. The calculated

thermodynamic parameters suggest that the inhibitor particles adsorb on the surface through an endothermic physisorption process.

5.- Data availability

The raw data required to reproduce these findings are available to download upon request.

The processed data required to reproduce these findings are available to download upon request.

6.- References

[1] R. B. Figueira, A. Sadovski, A.P. Melo, E. V. Pereira, *Constr. Build. Mater.* 2017,141,183.

[2] K. Byfors, *Cem. Concr. Res.*1987, 17, 115.

[3] S. M. Abd El Haleem, E. E. Abd El Aal, S. Abd El Wanees, A. Diab, *Corros. Sci.* 2010, 52, 3875.

[4] D. Rothstein; J. J. Thomas, B. J. Christensen; H. A. Jennings, *Cem. Concr. Res.* 2002, 32, 1663.

[5] P. Ghods; O. B. Isgor, G. McRae, T. Miller, *Cem. Concr. Compos.* 2009, 31, 2.

[6] S. M. Abd EL Haleem, S. Abd EL Wanees, EE. Abd EL Aal, A. Diab, *Corros. Sci.* 2010, 52, 292.

[7] M C. Alonso, M C. Andrade, *Corros. Sci.* 1989, 29, 1129.

[8] H. E. Jamil, M. F. Montemor, R. Boulif, A. Shiriri, M. G. S. Ferreira, *Electrochim. Acta.* 2003, 48, 3509.

[9] E.B. Castro, C.R. Valentini, C.A. Moina, J.R. Vilche, A.J. Arvia, *Corros. Sci.* 1986, 26, 781.

[10] L. Bertolini, F. Bolzoni, T. Pastore, *Corrosion.* 1996, 31, 218.

[11] T. A. ElMaaddawy, K. A. Soudki. *J. Mater. Civ. Eng.*, 2003, 15, 41.

- [12]. J. O. Okeniyi, O. A. Omotosho, O. O. Ajayi, C. A. Loto, *Constr. Build. Mater.* 2014, 50, 448.
- [13] M. B. Valcarcel, M. Vazquez, *Mater. Chem. Phys.* 2009, 115, 313.
- [14] G. T. Parthiban, T. Parthiban, R. Ravi, V. Saraswathy, N. Palaniswamy, V. Sivan, *Corros. Sci.* 2008, 50, 3329.
- [15] M. Manna, Effect of steel substrate for phosphate treatment, *Corros. Sci.* 2009, 51, 451.
- [16]. H. B. Gunay, P. Ghods, O. B. Isgor, G. J. C. Carpenter, X. Wu, *Appl. Surf. Sci.* 2013, 274, 195.
- [17] M. Behzadnasab, S.M. Mirabedini, K. Kabiri, S. Jamali, *Corros. Sci.* 2011, 53, 89.
- [18] R. Selvaraj, M. Selvaraj, S.V.K. Iyer, *Prog. Org. Coat.* 2009, 64, 454.
- [19] A. Canon, P. Garces, M. A. Climent, J. Carmona, E. Zornoza. *Corros. Sci.* 2013, 77, 128.
- [20] L. Fedrizzi, F. Azzolini, P. L. Bonora, *Cem. Concr. Res.* 2005, 35, 551.
- [21] P. Rodič, I. Milošev, *Corros. Sci.* 2019, 149, 108.
- [22] J. Sun, G. Wang, *Surf. Coat. Technol.* 2014, 254, 42.
- [23] Y. Kobayashi, Y. Fujiwara, *Electrochim. Acta.* 2006, 51, 4236.
- [24] E. Onofre-Bustamante, M.A. Dominguez-Crespo, J. Genescá-Llongueras, F.J. Rodríguez-Gómez, *Surf. Coat. Technol.* 2007, 201, 4666.
- [25] Y. Hamlaoui, F. Pedraza, C. Rémazeilles, S. Cohendoz, C. Rébéré, L. Tifouti, J. Creus, *Mater. Chem. Phys.* 2009, 113, 650.
- [26] J. Creus, F. Brezault, C. Rebere, M. Gadouleau, *Surf. Coat. Technol.* 2006, 200, 4636.
- [27] A. Montiel-García, E. Onofre Bustamante, M. L. Escudero-Rincón, E.C. De la Cruz-Terrazas, A. M. Torres-Huerta. *Cem. Concr. Compos.* 2018, 90, 202.
- [28] C. Casado, V. Nobel-Pujol, J. de Damborenea, *Cem. Concr. Compos.* 2006, 28, 267.
- [29] D. Guergova, E. Stoyanova, D. Stoychev, I. Avramova, P. Stefanov, *J. Rare Earths.* 2015, 33, 1212.

- [30] M. Ferreira, Jr., K. P. Souza, F. M. Queiroz, I. Costa, C. R. Tomachuk, *Surf. Coat. Technol.* 2016, 294, 36.
- [31] S.V. Harb, A. Trentin, T.A.C. de Souza, M. Magnani, S.H. Pulcinelli, C.V. Santilli, P. Hammer, *Chem. Eng. J.* 2020, 383, 123.
- [32] M. Gobara, A. Baraka, R. Akid, M. Zorainy, *Corrosion, RSC Adv.* 2020, 10, 2227.
- [33] P. Zhang, M. Zhu, W. Li, G. Xu, X. Huang, X. Yi, J. Chen, Y. Wu, *J. Rare Earths.* 2018, 36, 544.
- [34] J. Li, L. Ecco, A. Ahniyaz, M. Fedel, J. Pan, *J. Electrochem. Soc.* 2015, 162, C610.
- [35] M. F. Montemor, M. G. S. Ferreira, *Prog. Org. Coat.* 2008, 63, 330.
- [36] M. Fedel, A. Ahniyaz, L.G. Ecco, F. Deflorian, *Electrochim. Acta.* 2014, 131, 71.
- [37] R. Sharmila, N. Selvakumar, K. Jeyasubramanian, *Mater. Lett.* 2013, 91, 78.
- [38] D. D. Thiruvoth, M. Ananthkumar, *Materials Today: Proceedings*, 2022, 49, 2007.
- [39] T. Jima, K. Kato, T. Kuno, A. Okuwaki, Y. Umetsu, T. Okabe, *Ind. Eng. Chem. Res.* 1993, 32, 733.
- [40] A. B Corradi, F. Bondiol, A.M. Ferrari et al., *Mater. Res. Bull.* 2006, 41, 38.
- [41] A. Bumajdad, J. Eastoe, A. Mathew, *Adv. Colloid and Interface Sci.* 2009, 148, 56.
- [42] M. Yamashita, K. Kameyama, S. Yabe, S. Yoshida, Y. Fujishiro, T. Kawai, T. Sato, *J. Mater. Sci.* 2002, 37, 683.
- [43] L. G. Ecco, S. Rossi, F. Deflorian, M. Fedel, *J. Electrochem. Soc.* 2018, 165, C86.
- [44] M. Taguchi, S. Takami, T. Adschiri, T. Nakane, K. Sato, T. Naka, *Cryst. Eng. Comm.* 2011, 13, 2841.
- [45] R. Li, S. Yabe, M. Yamashita, S. Momose, S. Yoshida, S. Yin, T. Sato, *Solid State Ion.*, 2002, 151, 235.
- [46] F. Mansfeld, M. W. Kendig, S. Tsai, *Corrosion*, 1982, 38, 478.
- [47] G. Qiao, J. Ou, *Electrochim. Acta.* 2007, 52, 8008.

- [48] T. Eichler, B. Isecke, R. Babler, *Mater. Corros.* 2009, 60, 119.
- [49] L. Freire, M. J. Carmezim, M.G.S. Ferreira, M. F. Montemor, *Electrochim. Acta.* 2011, 56, 5280.
- [50] G. Liu, Y. Zhang, M. Wu, R. Huang, *Constr. Build. Mater.* 2017, 157, 357.
- [51] J-Y. Jiang, Y. Liu, H-Y.Chu, D. Wang, H. Ma, W. Sun, *Mater.* 2017, 10, 903.
- [52] B. Maniscalco, P. M. Kaminski, J. M. Walls, *Thin Solid Films.* 2014, 550, 10.
- [53] H. Boudellioua, Y. Hamlaoui, L. Tifouti, F. Pedraza, *J. Mater. Eng. Perform.* 2017, 26, 4402.
- [54] A. S. Umoren, A.Madhankumar, *J. Mol. Liq.* 2016, 224, 72.
- [55] H. Boudellioua, Y. Hamlaoui, L. Tifouti, F. Pedraza, *Mater. Corros.* 2020, 71, 1300.
- [56] M. Mobin, S. Zehra, R. Aslam, *RSC Adv*, 2016, 6, 5890.
- [57] T. Ngala, C. L. Page, M. M. Page, *Corros. Sci.* 2003, 45, 1523.
- [58] A. Rosenberg, C. Hansson and C. Andrade, Mechanisms of corrosion of steel in concrete, (1990). *Corrosion Rates of Steel in Concrete*, ed. N. Berke, V. Chaker, and D. Whiting (West Conshohocken, PA: ASTM International), 174-188.
<https://doi.org/10.1520/STP25023S>
- [59] E.A. Noor, A.H. Al-Moubaraki, *Mater. Chem. Phys.* 2008, 110, 145.
- [60] M. Znini, G. Cristofari, L. Majidi, A. Ansari, A. Bouyanzer, J. Paolini, J. Costa, B. Hammouti, *Int. J. Electrochem. Sci.* 2012, 7, 3959.
- [61] L.H Madkour, and S. K. Elroby, *Int. J. Ind. Chem.* 2015, 6, 165.
- [62] M. Hegazy, M. Abdallah, M. Alfakeer, H. Ahmed, *Int. J. Electrochem. Sci.* 2018, 13, 6824.
- [63] A. Popova, M. Christov, A. Vasilev, *Corros. Sci.* 2015, 94, 70.
- [64] R. Zandi Zand, K. Verbeken, V. Flexer, A. Adriaens, *Mater. Chem. Phys.* 2014, 145, 450.

Table1: Polarization parameters for the substrate immersed in saturated Ca(OH)₂ with 0.5 M CaCl₂ at room temperature with and without addition of inhibiting ceria nanoparticles.

Conc (ppm)	- E_{corr} (mV/SCE)	I_{corr} (μA/cm²)	β_a (mV/dec)	β_c (mV/dec)	R_p (Ω.cm²)	EI (%)
Blank	524	7.30	184.2	153.7	3162.00	-----
100	545	11.41	327.5	190.8	2060.62	-----
200	543	11.1	326.5	190.6	2218.19	-----
400	501	3.73	234.6	137.7	5610.47	48.94
600	484	3.03	289.4	143.1	7655.96	58.52
800	477	1.63	224.0	142.6	10519.61	77.68
1000	409	4.45	257.4	143.4	4008.66	39.09

Table 2: Fitting results for the EIS data for the substrate immersed in saturated Ca(OH)₂ with 0.5M CaCl₂ at room temperature with and without addition of inhibiting ceria nanoparticles.

Conc ppm	R_s Ω.cm²	CPE_{dc} μFs⁽ⁿ⁻¹⁾cm⁻²	n_{dc}	R_{ct} Ω.cm²	CPE_c mFsⁿ⁻¹cm⁻²	n_c	R_c Ω.cm²	R_d Ω.cm²	EI %
Blank	3.96	110.00	0.96	622.8	0.590	0.76	1297	----	-----
100	3.8	92.32	0.91	667.0	1.148	0.44	1636	88.1	6.62
200	3.92	81.60	0.91	775.2	0.74	0.44	1775	112.3	19.65
400	3.90	64.62	0.3	1763.0	0.596	0.41	6988	168.4	64.67
600	3.79	59.94	0.94	2789.0	0.324	0.42	7106	242.4	78.87
800	4.34	75.81	0.92	3282.0	0.217	0.45	7756	280.0	81.02
1000	4.31	70.78	0.94	989.6	0.780	0.44	5839	76.5	37.06

Table 3: Surface parameters of the substrate after polarization tests realized in saturated Ca(OH)_2 with 0.5M CaCl_2 at room temperature with and without addition of inhibiting ceria nanoparticles.

Conc ppm	Thickness (μm)	Grain size (μm)	Roughness (μm)
Blank	1.693	0.005	0.436
100	1.996	0.009	0.406
200	2.054	0.009	0.399
400	2.090	0.010	0.382
600	2.128	0.011	0.363
800	2.405	0.012	0.350
1000	2.340	0.012	0.353

Table 4: Fitting results for the EIS data for the substrate in saturated Ca(OH)₂ with 0.5M CaCl₂ without and with the presence of 800 ppm of ceria nanoparticles at different temperatures.

	TT (°C)	-E_{corr} (mV/ECS)	I_{corr} (μA/cm ²)	β_a (mV/dec)	β_c (mV/dec)	R_p (Ω.cm ²)	θ
Blank	20	-524	7.30	184.2	153.7	3162
	30	-501	7.62	151.6	224.4	1584
	40	-551	13.55	139.9	163.9	946
	50	-587	23.03	88.6	160.6	656
inhibitor	20	477	1.63	224.0	142.6	10519	0.77
	30	480	3.55	214.1	199.1	6426	0.53
	40	472	6.48	181.2	188.2	3054	0.52
	50	523	16.28	221.0	155.5	857	0.29

Table 5: Thermodynamic parameters for the substrate in saturated Ca(OH)₂ with 0.5M CaCl₂ with and without the presence of 800 ppm of ceria nanoparticles

	ΔH_a (kJ.mol ⁻¹)	ΔS_a (J.mol ⁻¹ .K ⁻¹)	Ea (kJ.mol ⁻¹)
Blank	28.87	-246.68	31.40
With ceria nanoparticles	56.44	-163.27	59.00

List of figure captions

Figure 1: Colour evolution during ceria nanoparticles preparation with increasing solution pH. (f) is the same pH 9.5 as (e) but has been maintained under magnetic agitation for 24 h.

Figure 2: SEM image (a) and FTIR spectrum (b) of synthesized ceria nanoparticles.

Figure 3: Polarization curves for the substrate immersed in saturated Ca(OH)_2 with 0.5M CaCl_2 at room temperature with increasing addition of inhibitor. N.B. “blank” had no inhibitor.

Figure 4: EIS diagrams (a) Nyquist and (b) phase plots for the substrate in saturated Ca(OH)_2 with 0.5 M CaCl_2 at room temperature with inhibitor addition. N.B. “blank” had no inhibitor.

Figure 5: Electrical equivalent circuit (EEC) model used for modelling EIS diagrams for the substrate in saturated Ca(OH)_2 with 0.5 M CaCl_2 at room temperature (a) without and (b) with addition of the inhibitor.

Figure 6: Optical macrographs showing the evolution of the surface of the substrate after polarization tests in saturated Ca(OH)_2 with 0.5 M CaCl_2 (a) without and with (b) 100 (c) 200 (d) 400 (e) 600 (f) 800 and (g) 1000 ppm of ceria nanoparticles at room temperature.

Figure 7: SEM images showing the evolution of the surface of the substrate after polarization tests in saturated Ca(OH)_2 with 0.5 M CaCl_2 at room temperature with and without (blank) inhibitor addition. EDS spectra of the surface of the substrate immersed in blank solution and of particles deposited on the surface of the substrate immersed in the solution with 800 ppm of ceria nanoparticles. N.B. “blank” had no inhibitor.

Figure 8: WLI (white- light interferometer; three- dimensional) images of the surface morphologies for the substrate after polarization test in in saturated Ca(OH)_2 with 0.5 M CaCl_2 at room temperature with and with inhibitor addition. N.B. “blank” had no inhibitor.

Figure 9: Polarization curves for the substrate immersed in saturated Ca(OH)_2 with 0.5 M CaCl_2 without (**a**) and with addition of 800 ppm of ceria nanoparticles (**b**) at different bath temperatures.

Figure 10: Arrhenius plots of mild steel immersed for 30 min in saturated Ca(OH)_2 with 0.5 M CaCl_2 solution with and without ceria nanoparticles.

Figure 11: SEM images showing the evolution of the surface of the substrate after polarization tests in saturated Ca(OH)_2 with 0.5 M CaCl_2 without (on the left) and in the presence of 800 ppm (on the right) at different bath temperatures.

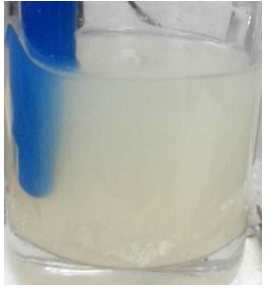
		
(a) pH 3.4	(b) pH 7	(c) pH 8
		
(d) pH 9	(e) pH 9.5	(f) pH 9.5

Figure 1:

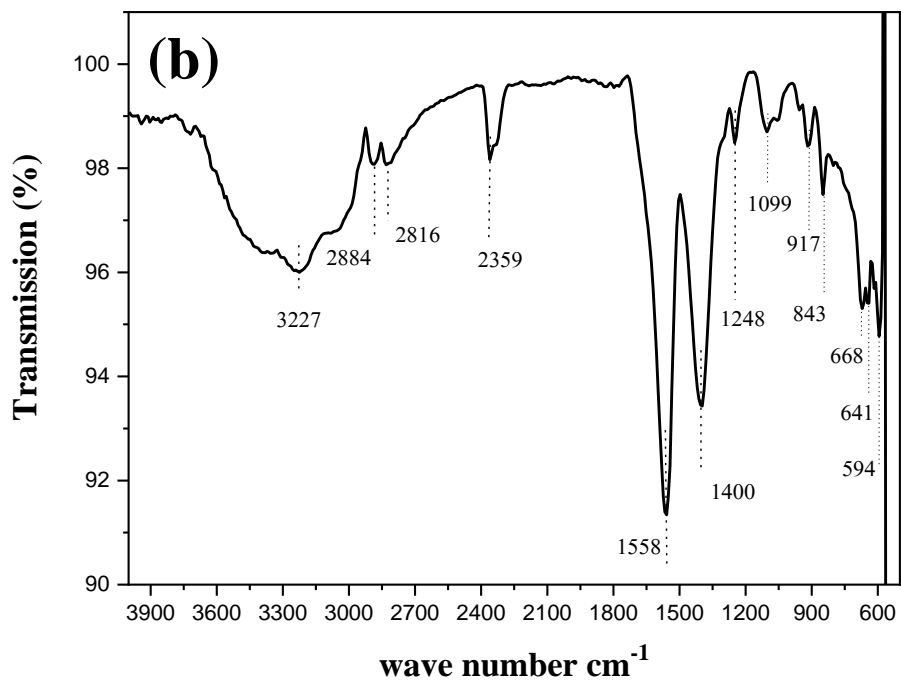
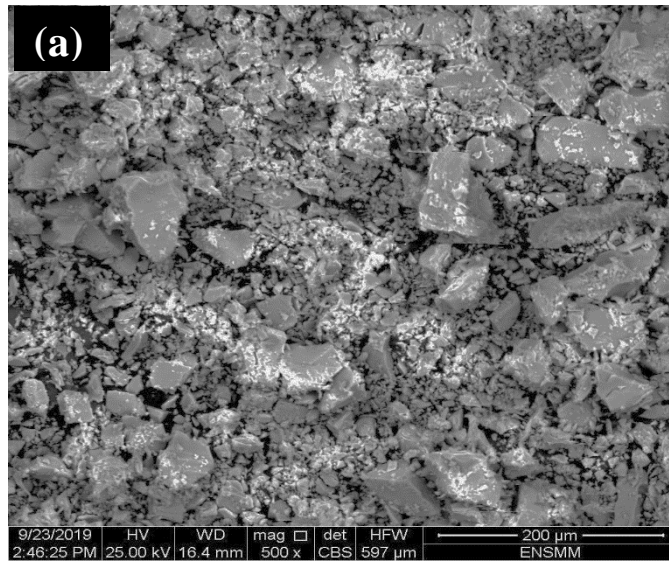


Figure 2:

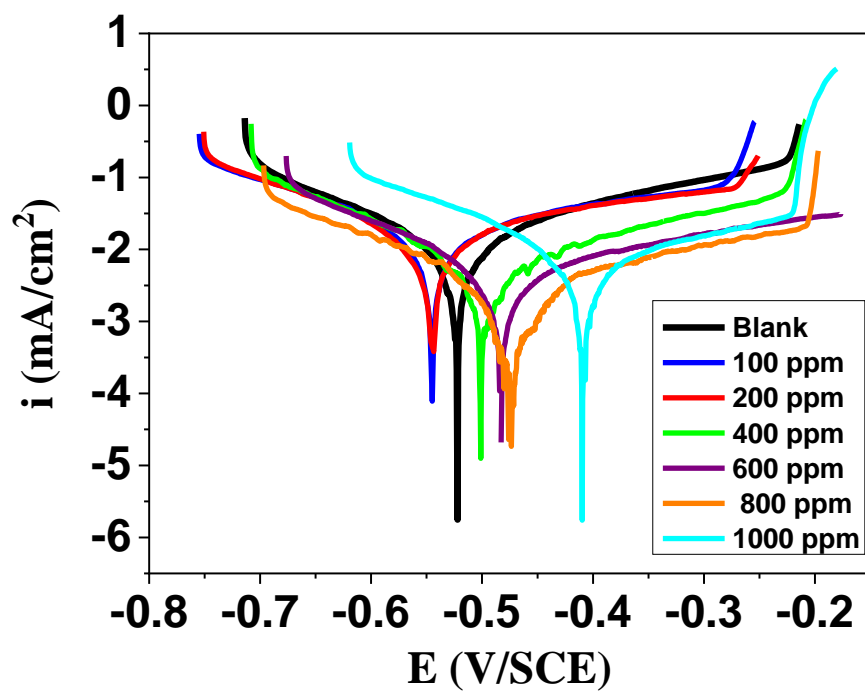


Figure 3:

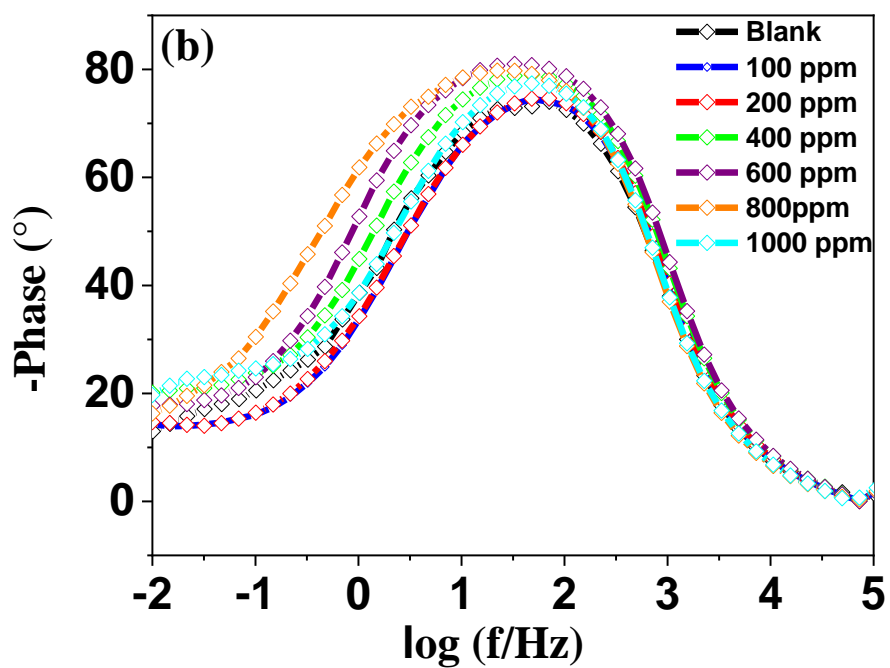
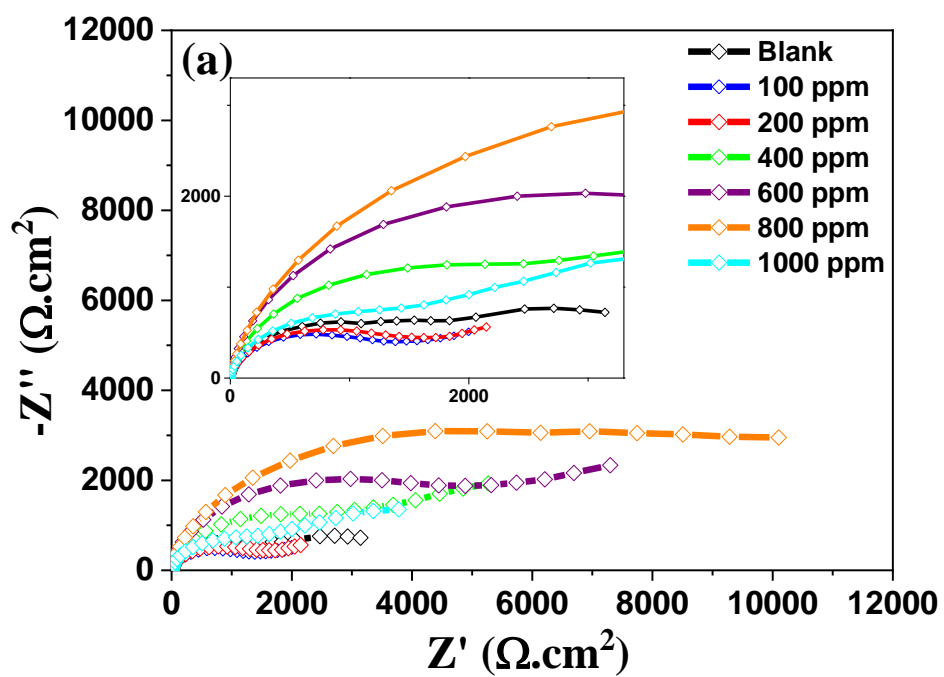


Figure 4:

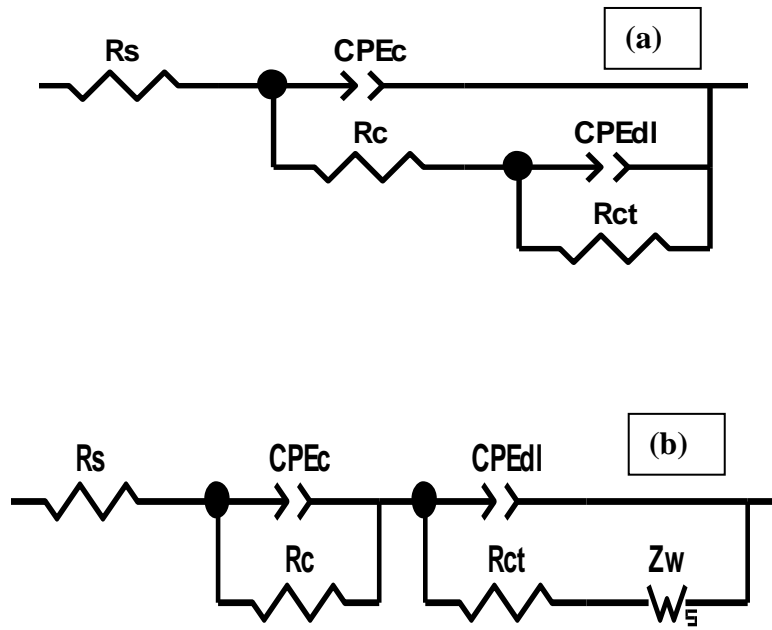


Figure 5:

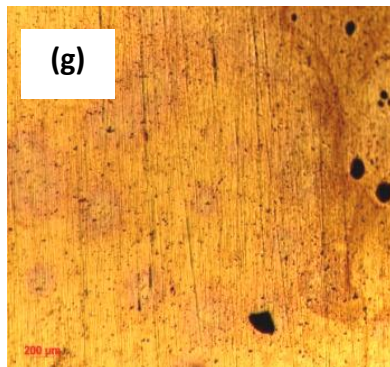
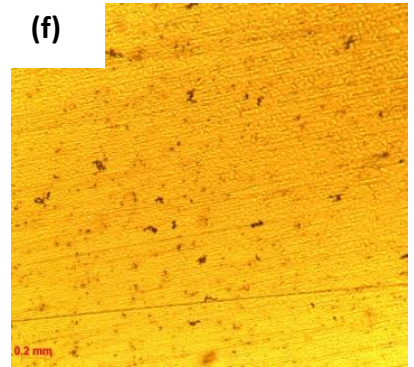
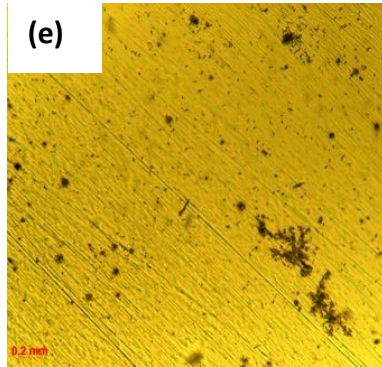
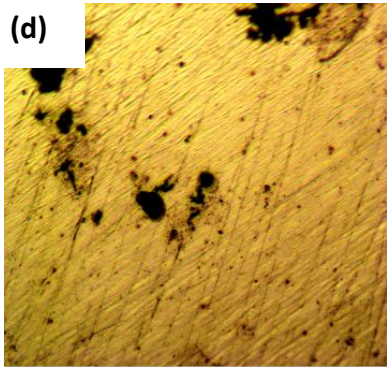
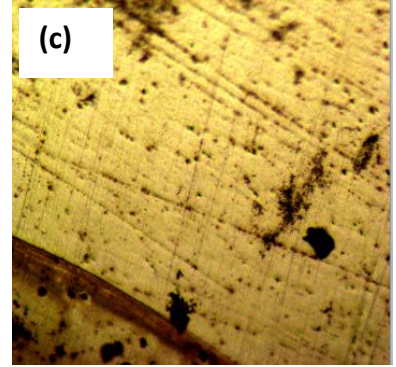
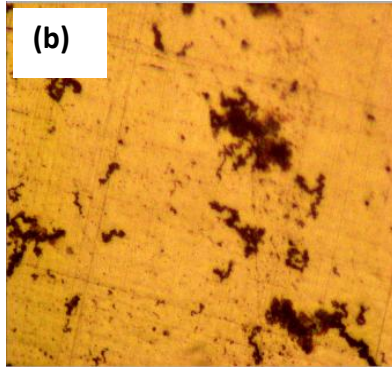
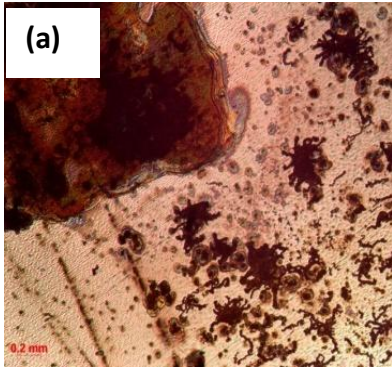


Figure 6:

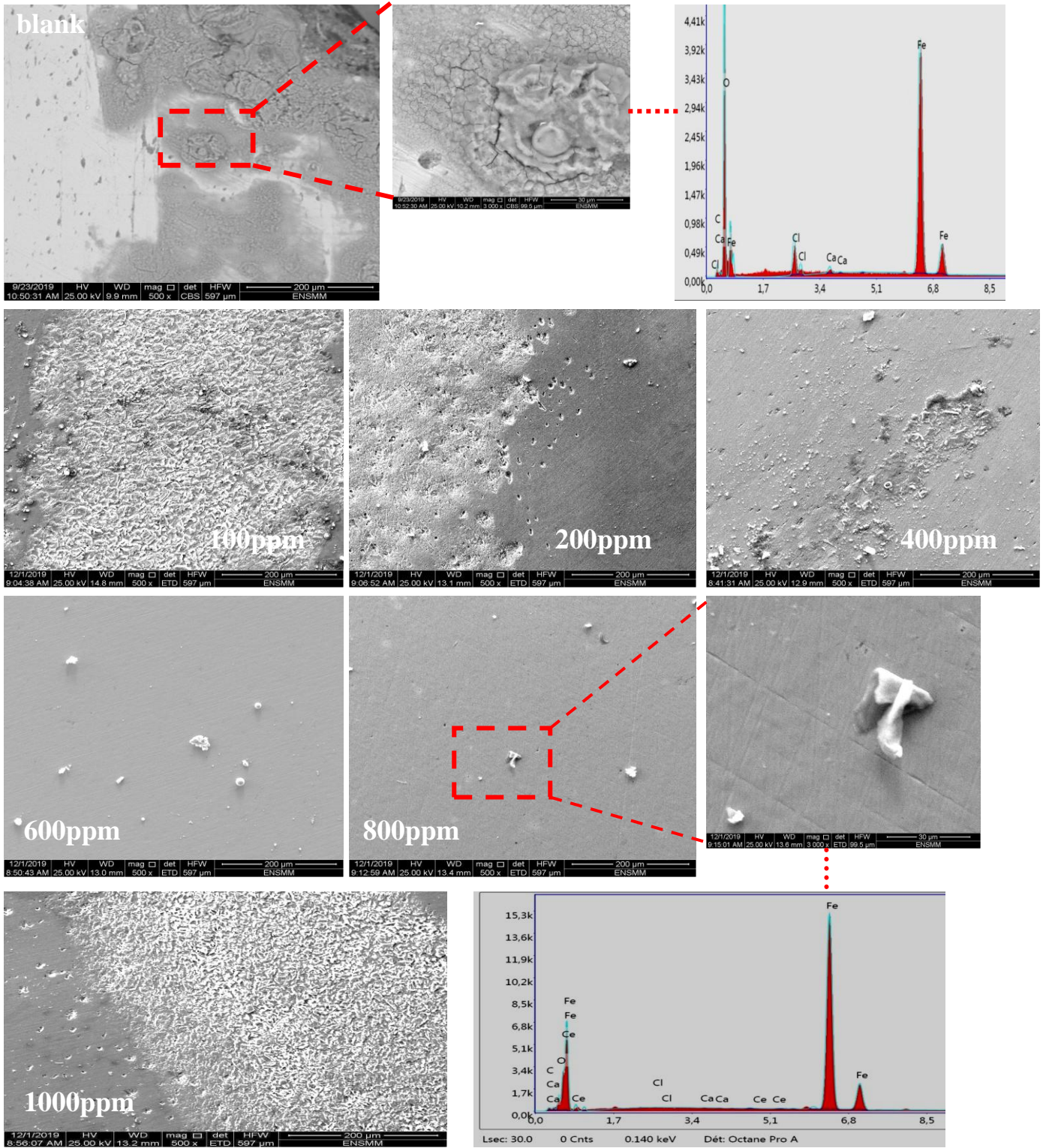


Figure 7:

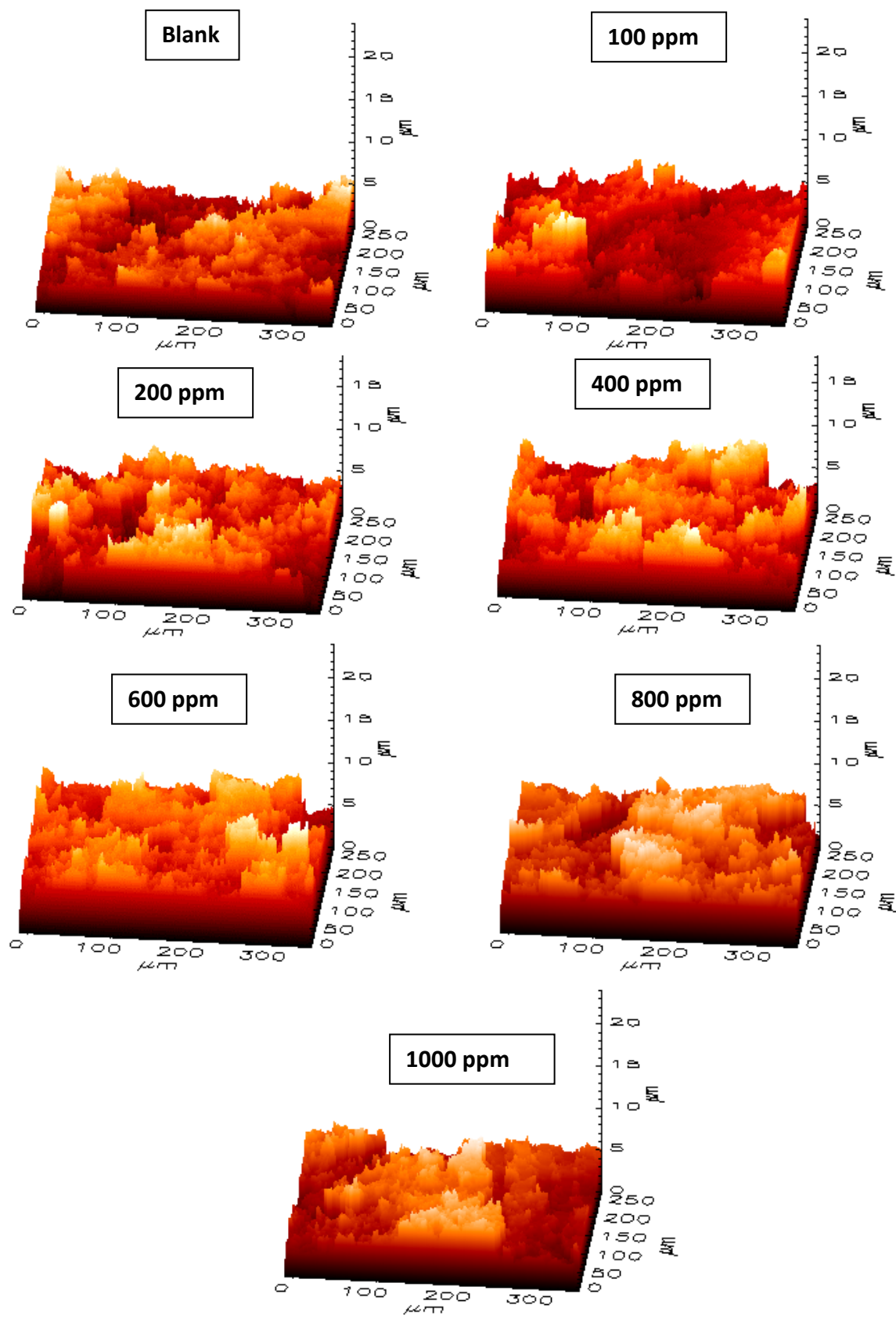


Figure 8:

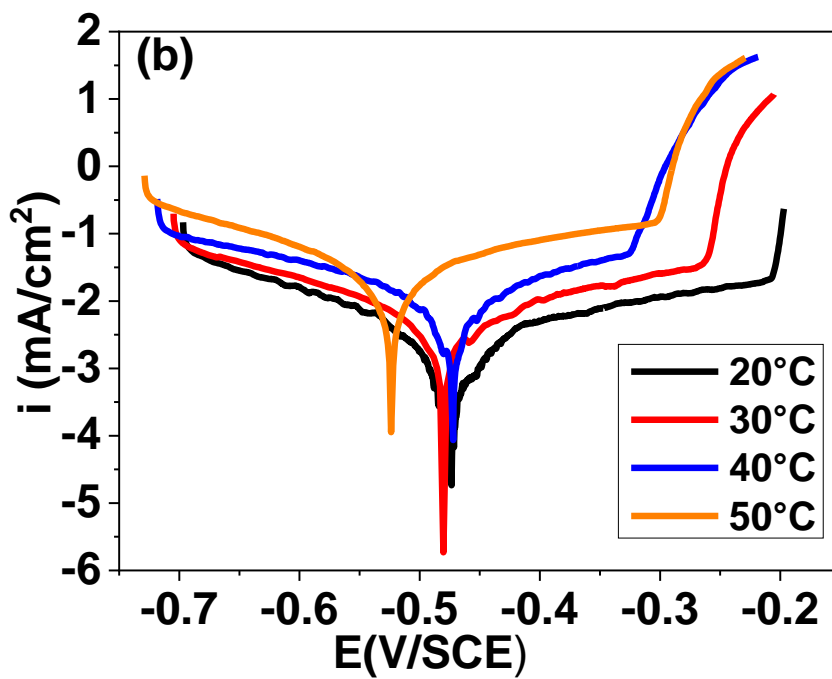
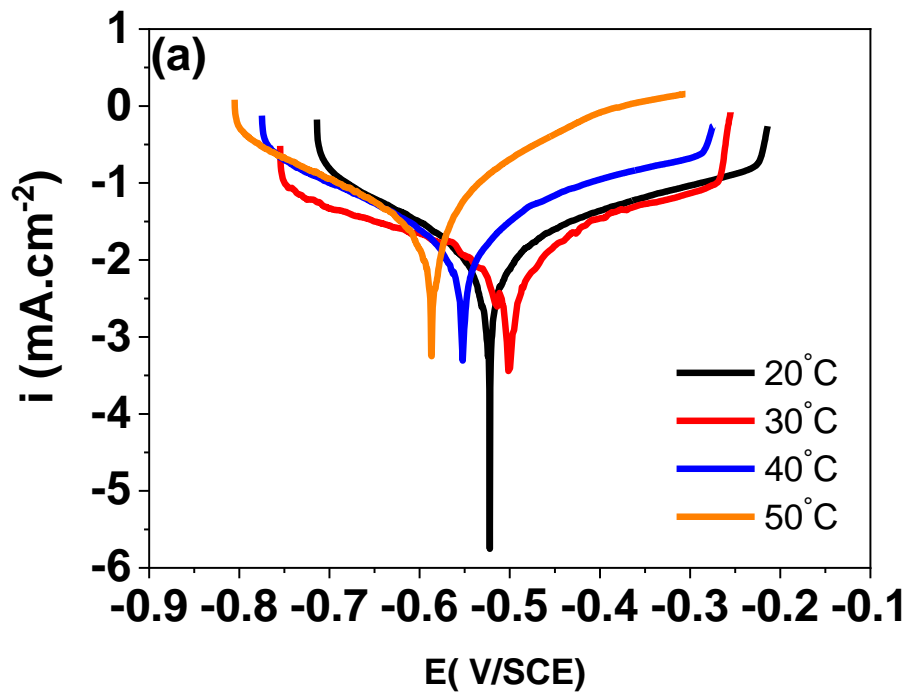


Figure 9:

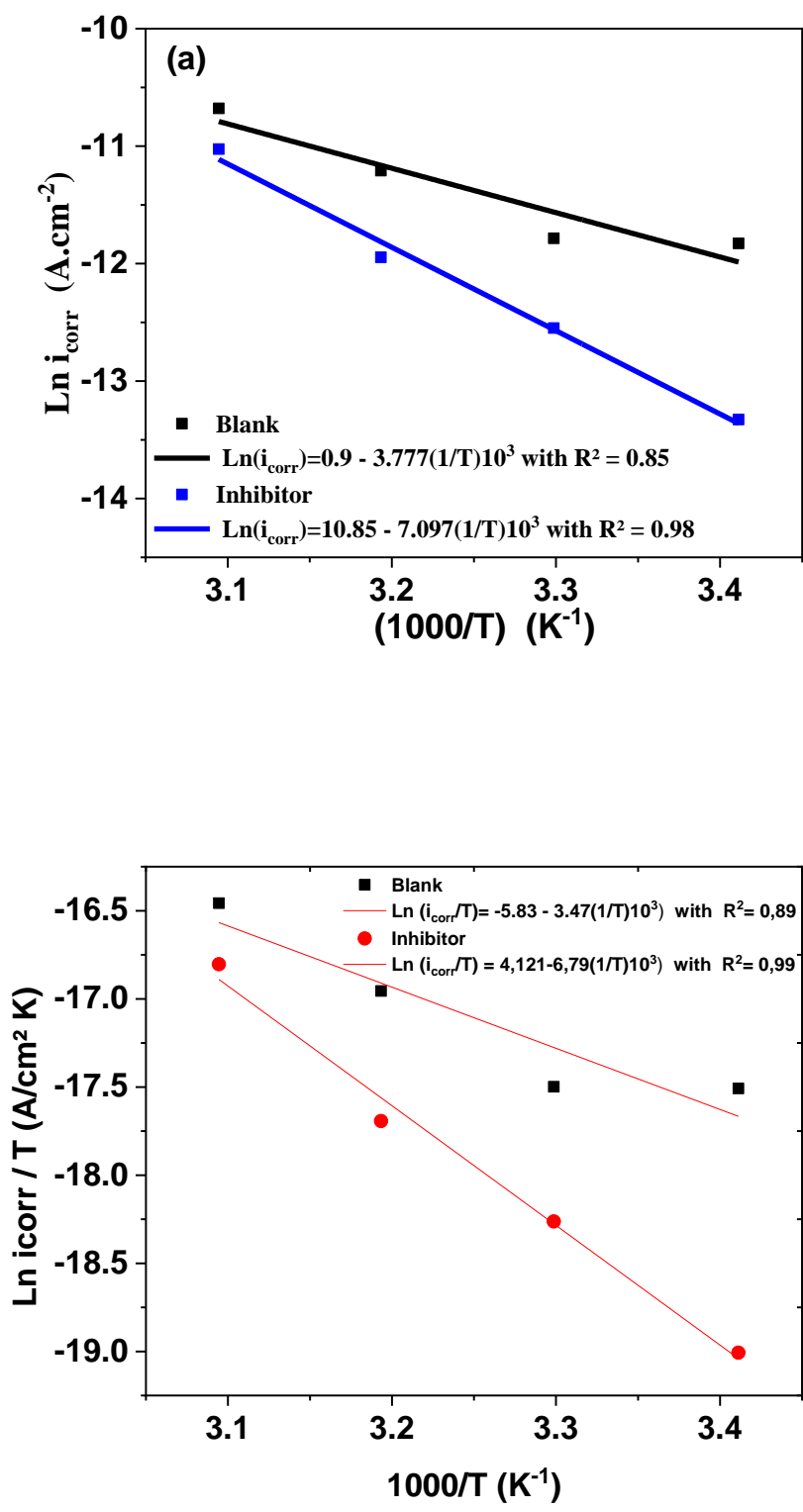


Figure 10:

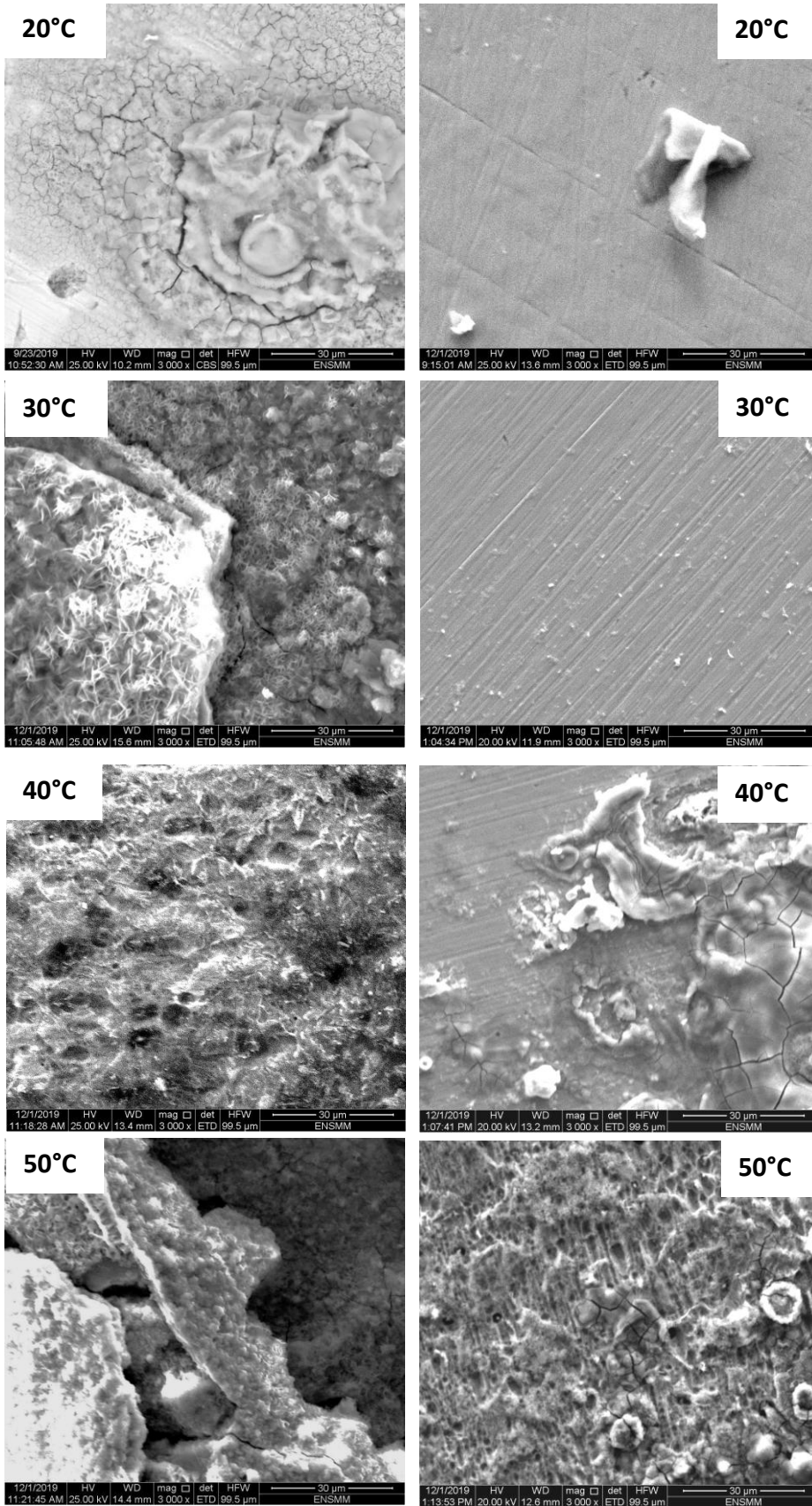


Figure 11: